




# Oxygen vacancies induced room temperature ferromagnetism and enhanced dielectric properties in Co and Mn co-doped ZnO nanoparticles

Zulfiqar<sup>1,2</sup>, Muhammad Zubair<sup>1</sup>, Aurangzeb Khan<sup>2,3</sup>, Tang Hua<sup>1,\*</sup>, Nasir Ilyas<sup>4</sup>, Simbarashe Fashu<sup>5</sup>, Amir Muhammad Afzal<sup>6</sup>, Main Akif Safeen<sup>7</sup>, and Rajwali Khan<sup>2,8,\*</sup> 

<sup>1</sup>School of Material Science & Engineering, Jiangsu University, Zhejiang 212013, China

<sup>2</sup>Department of Physics, Abdul Wali Khan University, Mardan 23200, KPK, Pakistan

<sup>3</sup>Vice chancellor of Lakki Marwat University, Lakki Marwat, KPK, Pakistan

<sup>4</sup>Department of Materials Science and Engineering, Guangdong Technion Israel Institute of Technology, Shantou 515063, Guangdong, China

<sup>5</sup>School of Optoelectronic Science and Engineering, University of Electronic Science and Technology of China, Chengdu 610054, China

<sup>6</sup>Department of Physics and Astronomy, Graphene Research Institute, Sejong University, Seoul 05006, Korea

<sup>7</sup>Department of Physics, University of Poonch, Rawalakot, Pakistan

<sup>8</sup>School of Physics and Optoelectronics Engineering, Shenzhen University, Nanshan 51800, Guangdong, China

Received: 24 October 2020

Accepted: 21 February 2021

Published online:

31 March 2021

© The Author(s), under exclusive licence to Springer Science+Business Media, LLC, part of Springer Nature 2021

## ABSTRACT

We investigated the influence of oxygen vacancies (varying) on the structure and properties (dielectric and magnetic) of Co (fixed) and Mn (varied) co-doped ZnO nanoparticles (NPs) fabricated using the chemical precipitation technique. The oxygen vacancies in the lattice increased with an increase in dopants (Co, Mn) concentration. Annealing of the doped nanoparticles decreased their dielectric properties due to reduced grain boundaries caused by enhanced grain growth. Replacement of Zn ions with dopants in the lattice enhanced the samples' electrical conductivities due to the reduction in grain boundaries and increase of charge carriers. The co-doped nanoparticles annealed at 600 °C exhibited some hysteresis loop changes and became ferromagnetic (FM). The magnetization increased with an increase in dopants content in the ZnO matrix, while coercivity decreased. This shows that the properties of the doped samples are strongly related to the number of oxygen vacancies. These results demonstrated that the enhanced dielectric and magnetization responses of Co (fixed) and Mn (varied) co-doped ZnO nanoparticles are strongly correlated with the oxygen vacancies. The enhancement in optical, dielectric, and magnetic

Zulfiqar and Muhammad Zubair contributed equally to this work.

Address correspondence to E-mail: [huatang79@163.com](mailto:huatang79@163.com); [rajwalipak@zju.edu.cn](mailto:rajwalipak@zju.edu.cn)

properties make transition metals (TM)-doped ZnO nanoparticles suitable for spintronics, and optoelectronic-based applications.

## 1 Introduction

Owing to their interesting applications, including in electronics, there is a renewed research interest in diluted magnetic semiconductors (DMS<sub>s</sub>) [1–7]. For them to meet the requirements, the DMS should display ferromagnetism (FM) at room temperature. So, to realize room temperature ferromagnetism (RTFM), many researchers worked on transition metals (TM)-doped II–VI semiconductors since they have excellent RTFM. The breakthrough started with Dietl et al. [7] in which RTFM was theoretically predicted, and this was later followed by many studies in doping semiconductors using magnetic ions. A semiconductor of significant importance is ZnO because of its excellent properties emanating from its ability to dissolve transition metals [8]. In particular, it has a wide bandgap and enormous binding energy, and these properties are of utmost importance in electronics. It has been doped with Fe ions transition metal at levels low enough that the structure is not changed and showed good properties. Several works have realized ferromagnetism in ZnO doped with TMs at curie temperatures ( $T_c$ ) higher than room temperature [8–10]. Because of this breakthrough, many scientists across the globe became interested in TMs-doped ZnO DMS [11, 12].

There are many techniques currently used to prepare TMs-doped ZnO nanoparticles, and these include thermal evaporation [13], vapor transport and condensation [14], ion implantation [15], pulsed-laser deposition [16], sol–gel [17], and hydrothermal method [18] and they are complicated processes. Among these techniques, the use of the hydrothermal route integrated with an electromagnetic field is a promising way for producing homogeneous dopants in ZnO nanoparticles. However, the drawback is that it requires special experimental conditions, like magnetic fields [19] and autoclaves [20]. The use of a strong magnetic field to enhance semiconductors magnetism through controlling the grain morphology in the hydrothermal process is now established and well documented [21, 22]. The use of a strong magnetic field was also shown to be good in

enhancing good precipitates distribution in the nanoparticle [23]. In our previous study [24], we have focused on diluted magnetic response of  $Zn_{0.96-x}Co_xMn_{0.04}O$  nanoparticles through the introduction of various concentrations of Co. We found that  $Zn_{0.96}Mn_{0.04}O$ ,  $Zn_{0.95}Mn_{0.04}Co_{0.01}O$ ,  $Zn_{0.94}Mn_{0.04}Co_{0.02}O$ , and  $Zn_{0.92}Mn_{0.04}Co_{0.04}O$  samples are ferromagnetic (FM) with good remnant magnetization ( $M_r$ ) and coercive field values by introducing oxygen vacancies on it [25]. The magnetic behavior of manganese and cobalt-doped ZnO was investigated by Jacek et al. It was found that with an increase in dopant concentration, there was a slight increase in ferromagnetism at 15 mol% doping level. Previously observed changes in chemical composition and lattice parameters demonstrate success in doping of ZnO nanoparticles with manganese and cobalt ions [26]. RTFM was reported by Babic-Stoji et al. [27] in ZnO samples annealed at low temperatures. The observed ferromagnetism was caused by contacts between manganese ions and defects. It was suggested that the observed magnetism was merely due to the material property of the doped nanoparticle and independent of other factors. Recent work reported RTFM in cobalt-doped ZnO nanoparticles [28]. RTFM was also observed in Fe [8], (Fe, Co) [29, 30], and Mn-doped [31] ZnO samples. There are many results on single doped ZnO to achieve the goal of RTFM but the co-doped ZnO nanomaterials are still lack focus.

Many experimental results showed that the role and effect of (co-doped TM ions)-ZnO nanoparticles on RTFM are not transparent, and, in some instances, there are some conflicts. To further clarify the mechanism, we report the variation in the structural, dielectric, and magnetic properties of ZnO (by introducing oxygen vacancies on it), when doped with Mn (varying) and Co (fixed).

## 2 Experimental method

The reagents used were zinc, manganese, and cobalt acetate, i.e.,  $Zn(CH_3COO)_2 \cdot 2H_2O$ ,  $Mn(CH_3COO)_2 \cdot 4H_2O$ , and  $Co(CH_3COO)_2 \cdot 6H_2O$ , respectively. The samples  $ZnO$ ,  $Zn_{0.87}Mn_{0.03}Co_{0.10}O$ ,

Zn<sub>0.84</sub>Mn<sub>0.06</sub>Co<sub>0.10</sub>O, and Zn<sub>0.81</sub>Mn<sub>0.09</sub>Co<sub>0.10</sub>O were prepared as follows: Firstly, 2.210 gm of Zinc acetate was dissolved into 100 ml deionized water. After that, 1.135 gm KOH was poured in 10 ml of deionized water. Then this solution was added to Zn (CH<sub>3</sub>COO)<sub>2</sub>·2H<sub>2</sub>O while mixing. It was then dried overnight in the oven to remove recrystallization water. White precipitates were obtained after the reaction. The precipitates were then washed several times under deionized water and annealed in a furnace at 600 °C for 4 h. For manganese and cobalt co-doped samples, we measured the required mass (gm) of Zinc acetate, Manganese acetate, and Cobalt acetate with a digital balance and then dissolved them into 100 ml distilled water following the same procedure used for pure ZnO.

The crystallographic information was obtained through X-ray diffraction (XRD) measurements using Cu K $\alpha$  radiation ( $\lambda = 1.5406 \text{ \AA}$ ). The Rietveld refinement technique was used to measure lattice parameters. The chemical composition was analyzed using an energy dispersive X-ray (EDX) spectroscopy attached to the Scanning Electron Microscopy (SEM) Instrumentation. Dielectric properties were carried out by Agilent Impedance Analyzer and LCR meter with a frequency range of 40 Hz–5 MHz. Magnetic properties of the samples were carried out by or Magnetic properties measurement system (MPMS) or Quantum Design superconducting Quantum interface Device (SQUID).

### 3 Results and discussion

XRD patterns for the samples were obtained using PANalytical-X'Pert [3] powder XRD and are shown in Fig. 1a, b. The XRD patterns for both samples show that they have the wurtzite structure (JCPDS card No. 36-1451). From the Rietveld refinement in Fig. 1a, the lattice parameters and unit cell volumes for different concentrations are shown in Table 1. The results show that with an increase in Mn content, the lattice parameters, as well as volume of the unit cell, were increased because the peaks shifted to the higher angles as shown in the inset of Fig. 1b. The microtensile strain and crystalline size of all samples are calculated from peak broadening by utilizing the Williamson–Hall plot as shown in Fig. 2 using the Eqs. 1, 2, 3.

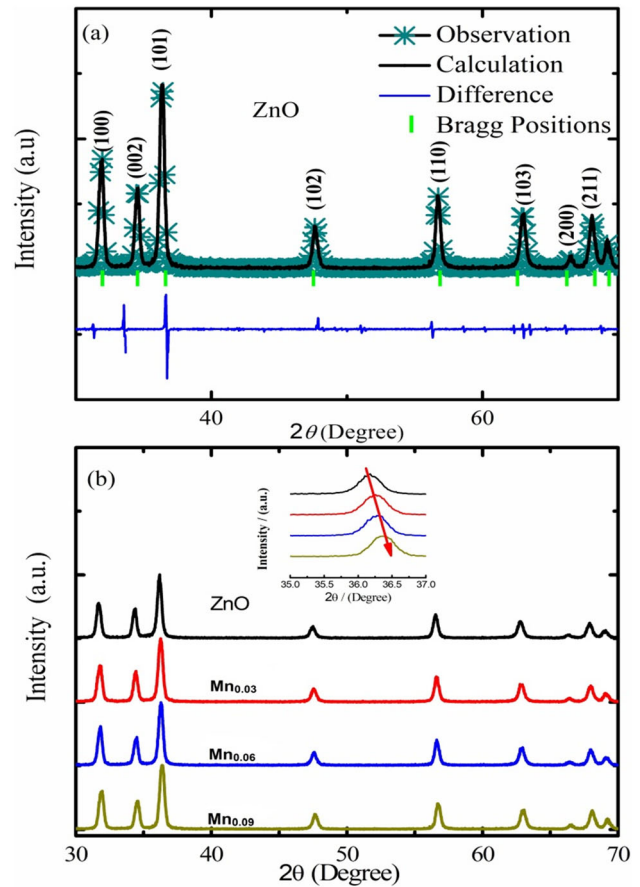


**Fig. 1** a X-ray diffraction Rietveld refinement (shown by the solid lines) of ZnO sample. b Powder X-ray diffraction patterns of ZnO, Zn<sub>0.87</sub>Mn<sub>0.03</sub>Co<sub>0.10</sub>O, Zn<sub>0.84</sub>Mn<sub>0.06</sub>Co<sub>0.10</sub>O, and Zn<sub>0.81</sub>Mn<sub>0.09</sub>Co<sub>0.10</sub>O samples

$$\beta = \beta_s + \beta_D \tag{1}$$

$$\beta = \frac{k\lambda}{D \cos\theta} + 4 \epsilon \tan\theta \tag{2}$$

$$\beta \cos\theta = 4 \epsilon \sin\theta + \frac{k\lambda}{D} \tag{3}$$

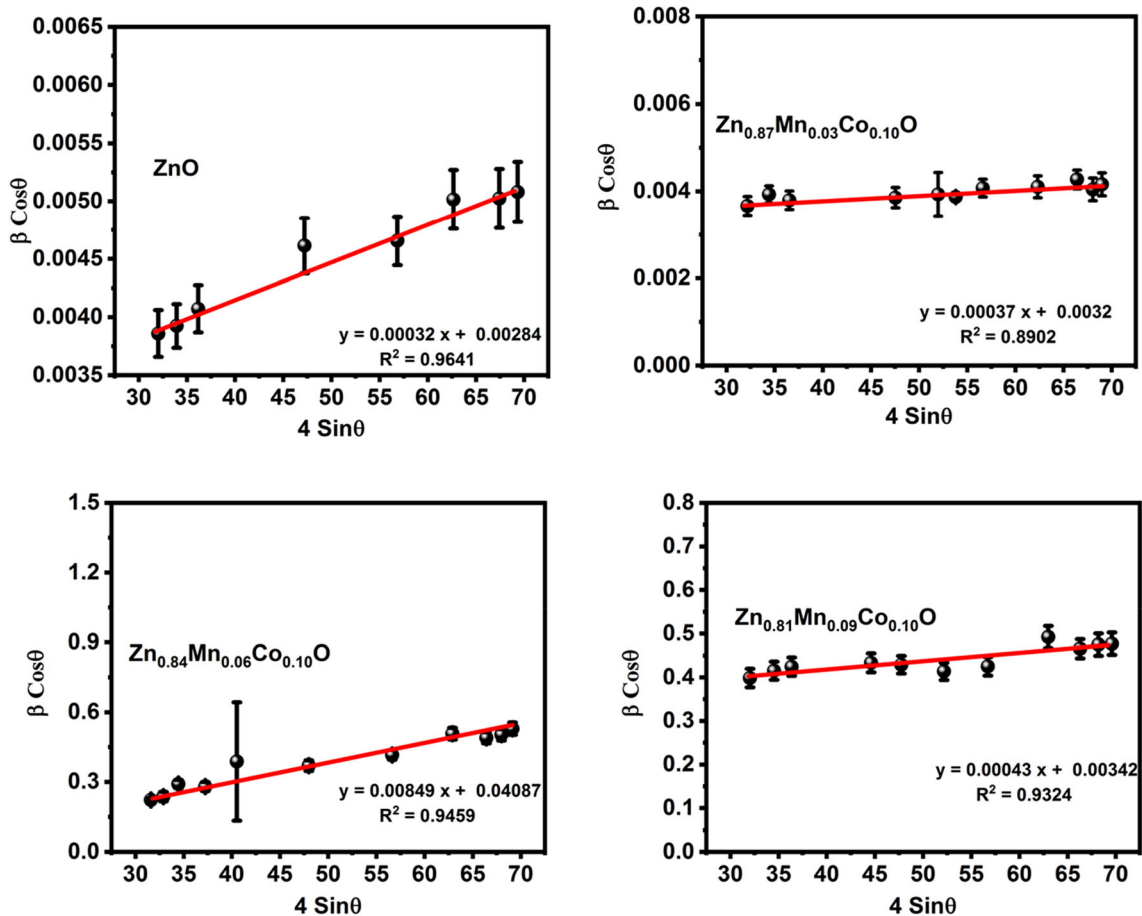
In Williamson–Hall plot assume that size and strain broadening are additive components of the total integral breadth of a Bragg peak as mentioned in the above equation. Strain-induced broadening arising from crystal imperfections and distortion are related by (as mention in Eq. 4).

$$\epsilon \approx \frac{\beta_s}{\tan\theta} \tag{4}$$

The crystallite size and lattice strain-dependent broadening are fitted by a curve for all the peak widths as a function of diffracting angle and FWHM

**Table 1** Structural parameters of ZnO, Zn<sub>0.87</sub>Mn<sub>0.03</sub>Co<sub>0.10</sub>O, Zn<sub>0.84</sub>Mn<sub>0.06</sub>Co<sub>0.10</sub>O, and Zn<sub>0.81</sub>Mn<sub>0.09</sub>Co<sub>0.10</sub>O samples calculated from XRD

Sample	(hkl)	d-spacing (Å)	2θ (°)	Crystallite size (nm)	Tensile strain	Lattice constant		Unit cell volume (Å) <sup>3</sup>
						a (Å)	c (Å)	
ZnO	(100)	2.5951	31.8885	48.26 ± 2.41	0.00032	3.2359	5.1848	47.06
	(002)	2.5894	34.5350	–	–	–	–	–
	(101)	2.4671	36.3850	–	–	–	–	–
(Mn <sub>0.03</sub> )	(100)	2.7958	31.9845	42.83 ± 2.14	0.00037	3.2447	5.1854	47.07
	(002)	2.5877	34.6348	–	–	–	–	–
	(101)	2.4601	36.435	–	–	–	–	–
(Mn <sub>0.06</sub> )	(100)	2.8044	31.8851	33.53 ± 1.67	0.00084	3.2451	5.1896	47.12
	(002)	2.5948	34.5363	–	–	–	–	–
	(101)	2.4671	36.3846	–	–	–	–	–
(Mn <sub>0.09</sub> )	(100)	2.7958	31.9850	40.31 ± 2.01	0.00043	3.2482	5.1754	46.11
	(002)	2.5877	34.6353	–	–	–	–	–
	(101)	2.4601	36.4358	–	–	–	–	–

**Fig. 2** Williamson–Hall Plot of all synthesized samples

for XRD peaks. The  $W-H$  graphs of the samples are plotted give the equation of a straight line,

$y = mx + c$  with slope equal to microstructural strain and the intercept from which the average crystallite

size is calculated as presented in Fig. 2 [32–34]. The incorporation of Mn and Co in the structure reduced the crystallite size from about 48.26 to 33.53 nm. Table 1 summarizes the quantitative data from XRD measurements. In this case, the lattice sizes increase with an increase in Mn and Co contents in the ZnO structure because of higher ionic radii of  $\text{Mn}^{2+}$  (0.80 Å) and  $\text{Co}^{2+}$  (0.65 Å) as compared to  $\text{Zn}^{2+}$  (0.60 Å). The differences in radius cause ZnO lattice distortion and the tensile strain increases. The decrease in crystallite size and increase in tensile strain introduce oxygen vacancies (defect density) to the ZnO lattice with increasing dopants concentration. The minimum crystallite size and maximum tensile strain are reported for  $\text{Zn}_{0.84}\text{Mn}_{0.06}\text{Co}_{0.10}\text{O}$ , which means defect density (oxygen vacancies) is maximum in this sample. However, the authors observed a decrease in lattice constants with an increase in Mn doping ( $x = 0.09\%$ ) in ZnO matrix because of the formation of  $\text{Mn}^{3+}$  and  $\text{Mn}^{4+}$  ions [35]. The observed shifting of peak positions in co-doped samples are in agreement with changes in lattice sizes, and the finding agrees with the explanation that the  $\text{Mn}^{2+}/\text{Co}^{2+}$  ions substitute  $\text{Zn}^{2+}$  in the ZnO structure. The ratios of lattice parameters ( $c/a$ ) do not change enough, and this confirms that the dopants are well accommodated and the structure is unchanged.

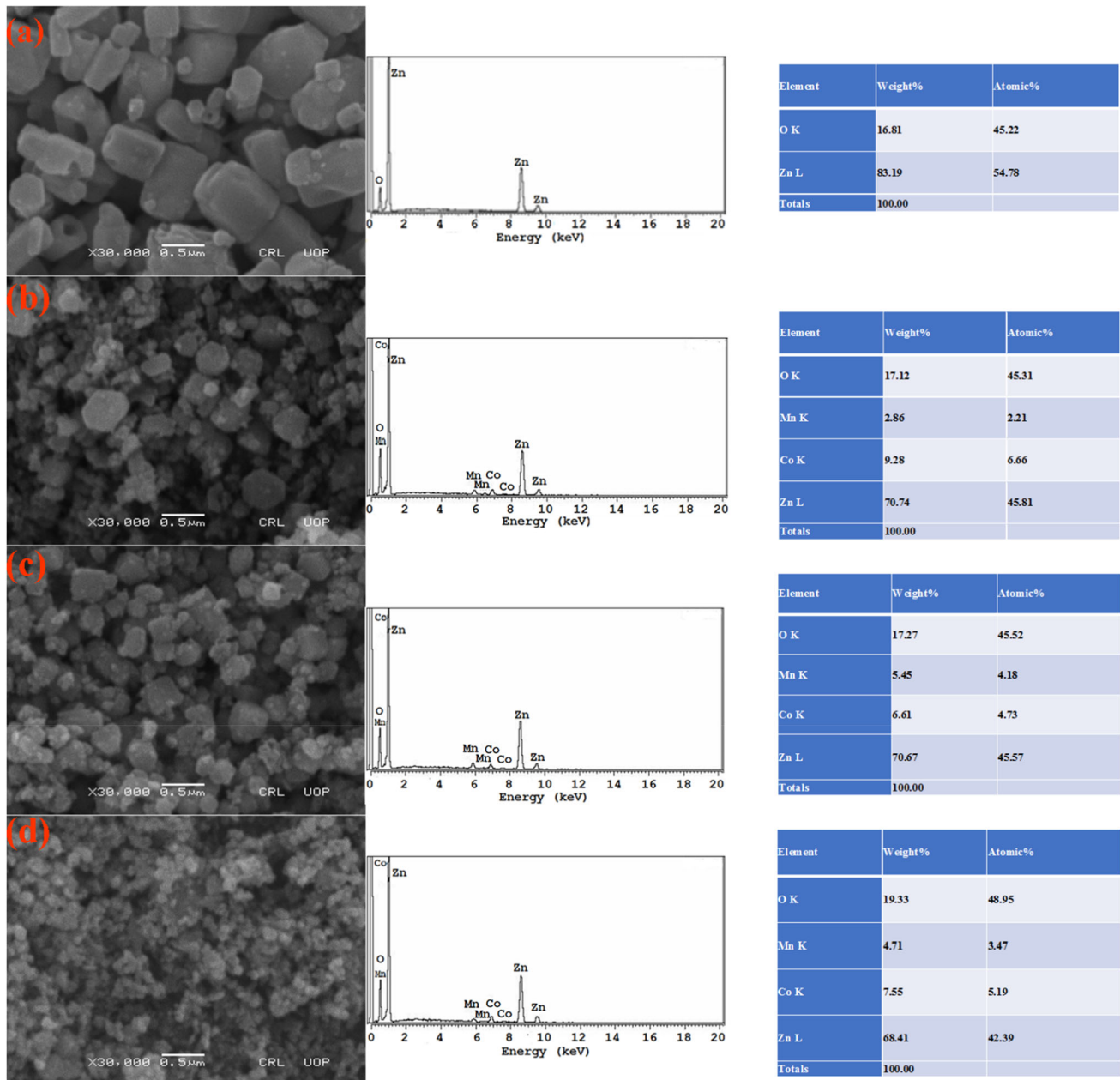
The Scanning Electron Microscopy (SEM) Instrumentation images for all the samples are shown in Fig. 3a–d, while the corresponding overall EDS spectra are shown on the right side of Fig. 3a–d. High crystallinity with the rod-shaped structure of pure ZnO nanoparticles can be seen in Fig. 3a with the corresponding EDS spectra on the right side (Fig. 3a) having Zn and O peaks with 83.19 wt% and 16.81 wt%, respectively. The crystallinity was found to decrease with an increase in co-dopants' concentration, which is in agreement with the XRD results. The results show that particle agglomeration increases with an increase in doping concentration, and sheet-like structure appeared (Fig. 3b–d). The Zn elemental weight percent decreased with an increase in dopants concentration as evident from the EDS spectra. The elemental weight percent accompanying EDS peaks for Zn, O, Mn and Co are given in Fig. 3b–d, showing that the oxygen content of the samples continuously reduced as compared to pure ZnO [36].

Figure 4 shows the FTIR spectra for ZnO and doped samples measured at room temperature.

High-intensity absorption peaks for ZnO are at 645, 662, and  $800\text{ cm}^{-1}$ . Two peaks observed at  $1624$  and  $3436\text{ cm}^{-1}$  are due to O–H stretching and H–O–H bending vibrations and can be assigned to small amounts of  $\text{H}_2\text{O}$  present in nanocrystalline ZnO. The presence of carbon dioxide from the atmosphere produced a peak at  $2386\text{ cm}^{-1}$ . Bond stretching in ZnO causes a weak peak at  $512\text{ cm}^{-1}$ . Similarly, in the  $\text{Zn}_{0.87}\text{Mn}_{0.03}\text{Co}_{0.10}\text{O}$  sample, peaks at  $1390\text{ cm}^{-1}$  and  $2333\text{ cm}^{-1}$  are due to bond and symmetric stretching, respectively. While, in  $\text{Zn}_{0.84}\text{Mn}_{0.06}\text{Co}_{0.10}\text{O}$  sample, peaks  $662\text{ cm}^{-1}$  and  $1395\text{ cm}^{-1}$  are assigned to O–H asymmetric stretching [36].

The UV–Vis absorption spectra recorded (200 to 1000 nm) by dispersing sample in the ethanol as shown in Fig. 5. The absorption peaks were found to be at 380 nm for ZnO, at 375 nm for  $\text{Zn}_{0.87}\text{Mn}_{0.03}\text{Co}_{0.10}\text{O}$ , at 393 nm for  $\text{Zn}_{0.84}\text{Mn}_{0.06}\text{Co}_{0.10}\text{O}$ , and at 389 nm for  $\text{Zn}_{0.84}\text{Mn}_{0.09}\text{Co}_{0.10}\text{O}$  and this shows the shifting in the joint curve due to co-doping in ZnO. The absorbance increases with increasing Mn concentration and it is maximum for  $\text{Zn}_{0.84}\text{Mn}_{0.06}\text{Co}_{0.10}\text{O}$  sample, revealing large number of oxygen vacancies (defects) in the sample. The bandgap energies calculated using Tauc's plot are  $2.55 \pm 0.13\text{ eV}$ ,  $2.7 \pm 0.14\text{ eV}$ ,  $2.40 \pm 0.13\text{ eV}$ , and  $2.54 \pm 0.12\text{ eV}$  for ZnO,  $\text{Zn}_{0.87}\text{Mn}_{0.03}\text{Co}_{0.10}\text{O}$ ,  $\text{Zn}_{0.84}\text{Mn}_{0.06}\text{Co}_{0.10}\text{O}$ , and  $\text{Zn}_{0.81}\text{Mn}_{0.09}\text{Co}_{0.10}\text{O}$  as shown in Fig. 5. These results are in agreement with the previous results [36]. The bandgap energies and crystallite size are plotted against Mn concentration and the minimum values of both crystallite size and bandgap are found for the  $\text{Zn}_{0.84}\text{Mn}_{0.06}\text{Co}_{0.10}\text{O}$  sample, which is due to presence of large number of oxygen vacancies.

Figure 6 shows the PL spectra of ZnO and doped nanoparticles in the wavelength range of 300–800 nm with excitation wavelength of  $\lambda_{\text{ex}} = 275\text{ nm}$ . The corresponding magnified PL spectra are shown in the inset of Fig. 6. Sharp peaks of 326, 380 and 386 nm are observed corresponding to band to band transition. High and low-intensity peaks at 405, and 412 nm, respectively, are for the violet band region. Besides, peaks at 419, 425, 440, and 448 nm correspond to the violet emission while those at 483 nm, and 492 nm correspond to the blue-green emission. In the green emission region, peaks of 510, and 518 nm are observed. The PL graph for  $\text{Zn}_{0.81}\text{Mn}_{0.09}\text{Co}_{0.10}\text{O}$  in Fig. 6 shows that the peak intensity is lowest compared to the other three samples as shown the inset of Fig. 6. A sharp peak at 326 nm is for the ultraviolet



**Fig. 3** a–d SEM images and their corresponding EDS of ZnO,  $\text{Zn}_{0.87}\text{Mn}_{0.03}\text{Co}_{0.10}\text{O}$ ,  $\text{Zn}_{0.84}\text{Mn}_{0.06}\text{Co}_{0.10}\text{O}$ , and  $\text{Zn}_{0.81}\text{Mn}_{0.09}\text{Co}_{0.10}\text{O}$  nanoparticles

(UV) region, and this also shows that the peak shifts to a longer wavelength. The peaks corresponding to 405, 416, 422, 429 and 443 nm are for the violet while the 490 nm peak is for the blue-green emission. Peaks of 508, 514, 526 and 545 nm correspond to the green emission, while a peak of 556 nm was observed for the yellow-green emission. Peaks of 592, 612, and 616 nm are assigned to the orange emission and the high-intensity peak at 653.3 nm is in the visible region [36].

The hysteresis ( $M-H$ ) loops of co-doped ZnO NPs measured at room temperature are shown in Fig. 7a and the inset of Fig. 7a shows the  $M(H)$  curve near zero magnetic field. The figure shows that ZnO exhibit diamagnetism (data not shown here) at 300 K, while co-doped samples are ferromagnetic (FM). For  $\text{Zn}_{0.87}\text{Mn}_{0.03}\text{Co}_{0.10}\text{O}$ ,  $\text{Zn}_{0.84}\text{Mn}_{0.06}\text{Co}_{0.10}\text{O}$  and  $\text{Zn}_{0.81}\text{Mn}_{0.09}\text{Co}_{0.10}\text{O}$  samples, the remnant magnetization ( $M_r$ ) values are  $\sim 0.27$ , 1.7, 1.28 emu/g, and corresponding coercive field values are 97Oe, 45Oe, and 50

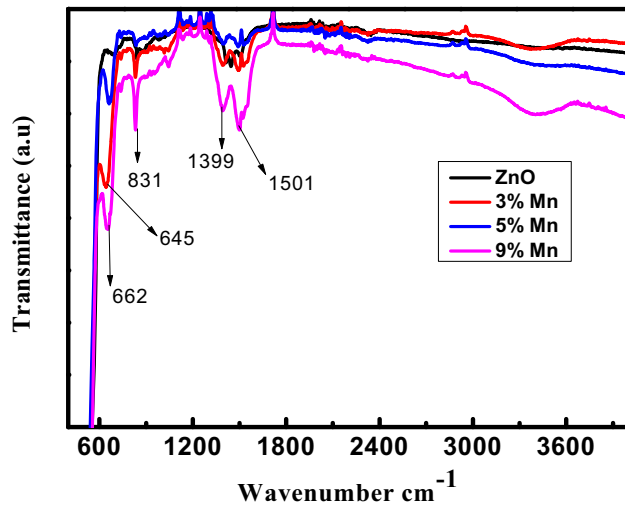


**Fig. 4** Fourier Transform Infrared Spectra of ZnO,  $\text{Zn}_{0.87}\text{Mn}_{0.03}\text{Co}_{0.10}\text{O}$ ,  $\text{Zn}_{0.84}\text{Mn}_{0.06}\text{Co}_{0.10}\text{O}$ , and  $\text{Zn}_{0.81}\text{Mn}_{0.09}\text{Co}_{0.10}\text{O}$  samples

Oe (Fig. 7b), respectively. This shows that the observed  $M_r$  value of the  $\text{Zn}_{0.84}\text{Mn}_{0.06}\text{Co}_{0.10}\text{O}$  is higher than the one obtained in Ref. [25]. Figure 7 shows that the highest saturation magnetization ( $M_s$ ), and  $M_r$  are observed at 6% Mn since Mn and Co spins will be ferromagnetically coupled [37]. The remnant magnetization and saturation magnetization increases, while coercivity is reduced with the increase in the concentration of Mn (dopant) from 3 to 9% in the  $\text{Zn}_{1-x}\text{Mn}_x\text{Co}_{0.10}\text{O}$  matrix. The increase in  $M_r$  is attributed to an increase in density of oxygen vacancies [38]. This occurs because of the migration of  $\text{O}^{2-}$  ions from the lattice, and the formation of oxygen vacancies near Mn and Co-doped ions to balance charge [39]. The resulting magnetization is due to bound magnetic polarons (BMPs) [40]. Mutual interaction of high-density BMPs (due to large content of oxygen vacancies) forms magnetic domains with long-range ferromagnetic ordering. Magnetization increases with an increase in Mn content because the parallel spin–spin coupling between Mn and Co ions is more favorable than antiparallel coupling. Nearby oxygen atoms result in charge carrier exchange between oxygen vacancies and Co/Mn ions [41]. An increase in  $M_s$  and  $M_r$  and reduction in coercive  $H_c$  with an increase in Mn content (Fig. 7b) are both caused by the high density of oxygen vacancies.

To find the exact  $T_C$ , the magnetization behaviors versus temperature response of the co-doped ZnO were studied using a 1000 Oe magnetic field (Fig. 7c).

The Figure shows that the 6% Mn co-doped ZnO sample has the highest FM behavior compared to those with only Mn or higher Co contents, as clearly displayed in Fig. 7d. The ferromagnetic coupling between TM ions and bound polarons forms bound magnetic polarons [42] and this is how FM originates in TM-doped ZnO [43, 44]. Some previous studies about carriers in point defects show that both hybridization and TM substitutions induce RTFM in doped ZnO [33, 45–47]. This work showed that the substitution of Manganese and Cobalt ions into the ZnO lattice introduces a large number of oxygen vacancies (defects). In  $\text{Zn}_{0.84}\text{Mn}_{0.06}\text{Co}_{0.10}\text{O}$  nanoparticles, a large number of oxygen vacancies is formed by the replacement of  $\text{Zn}^{2+}$  with  $\text{Mn}^{2+}$  and  $\text{Co}^{2+}$  ions along with the formation of oxygen vacancies to enhance RTFM. The phenomenon is novel and related to RTFM introduced during sample preparation through (Mn, Co) co-doping. The origins of the observed magnetism at low temperatures should be investigated in detail.

The changes in dielectric constant ( $\epsilon_r$ ) for ZnO,  $\text{Zn}_{0.87}\text{Mn}_{0.03}\text{Co}_{0.10}\text{O}$ ,  $\text{Zn}_{0.84}\text{Mn}_{0.06}\text{Co}_{0.10}\text{O}$ , and  $\text{Zn}_{0.81}\text{Mn}_{0.09}\text{Co}_{0.10}\text{O}$  NPs annealed at 600 °C are shown in Fig. 8a. The graph shows that the values of  $\epsilon_r$  decreases with an increase in frequency up to  $1 \times 10^6$  Hz and then remains constant at higher frequencies. The sample powder was compacted using a 9 mm diameter presser to fabricate circular-shaped pellets and Gold glue was pasted on pellets as an electrode to measure the capacitance, dielectric loss, and conductivity variations with frequency. A similar approach was used by Khan et al. [19, 24, 32, 48]. The following mathematical formula (5) was used to calculate the dielectric constant:

$$\epsilon_r = Cd/\epsilon_0 A \quad (5)$$

$\epsilon_r$ ,  $C$ ,  $d$ ,  $A$ , and  $\epsilon_0$ , respectively are for sample relative dielectric constant, capacitance, height, pellet cross-sectional area, and space dielectric constant. Results show that the  $\epsilon_r$  values for the ZnO,  $\text{Zn}_{0.87}\text{Mn}_{0.03}\text{Co}_{0.10}\text{O}$ ,  $\text{Zn}_{0.84}\text{Mn}_{0.06}\text{Co}_{0.10}\text{O}$  and  $\text{Zn}_{0.81}\text{Mn}_{0.09}\text{Co}_{0.10}\text{O}$  samples calcined at 600 °C rapidly decreases as frequency increases up to  $1 \times 10^4$  Hz before remaining constant. Rotation dielectric polarization (RDP) and space charge polarization (SCP) may be used to explain this behavior. This is mainly based on the presence of a high density of oxygen vacancies [45]. Then differently charged vacancies form randomly oriented dipole moments which are easy to polarize.

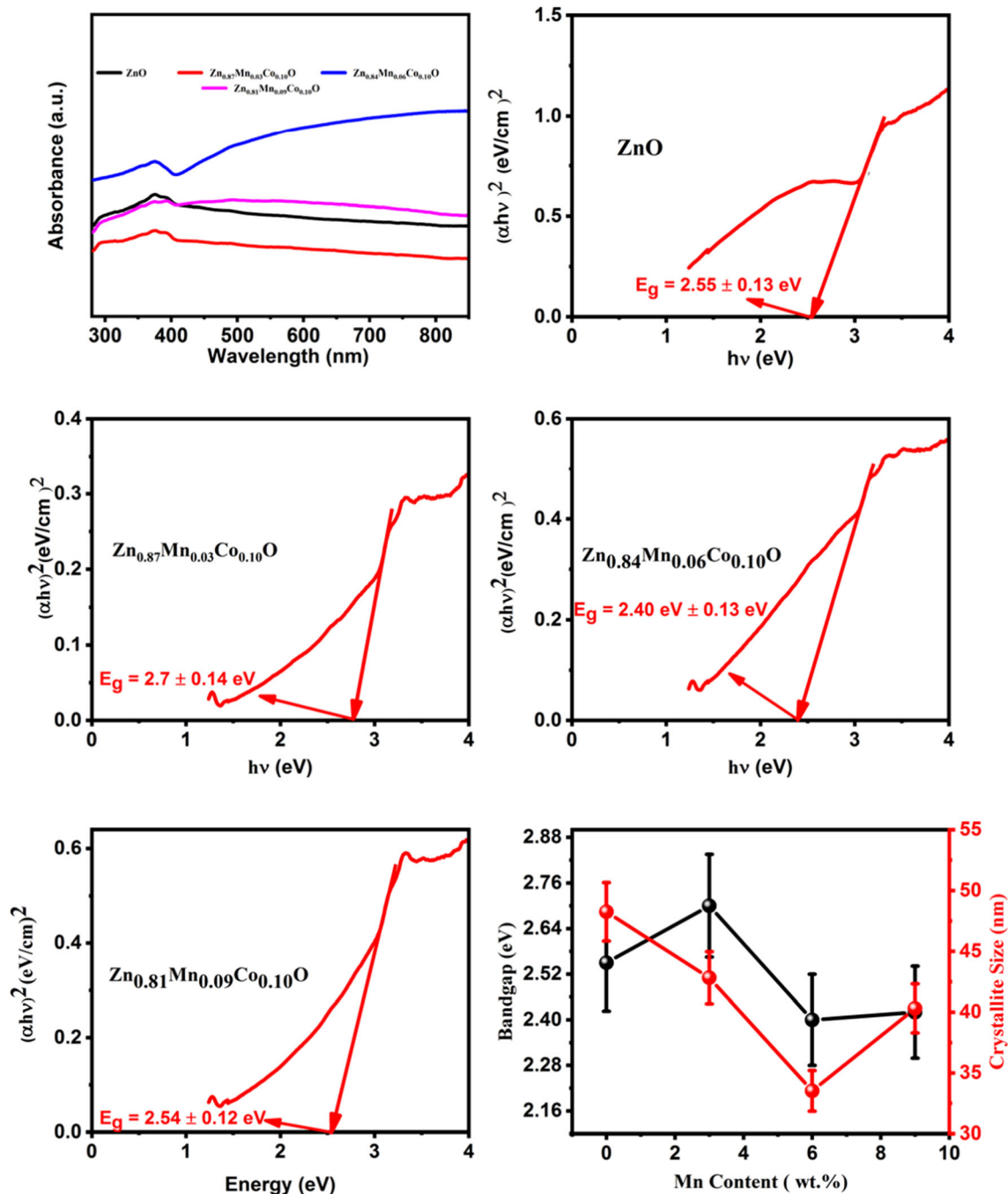


**Fig. 5** Absorbance spectra, and the calculated Bandgap energies of ZnO, Zn<sub>0.87</sub>Mn<sub>0.03</sub>Co<sub>0.10</sub>O, Zn<sub>0.84</sub>Mn<sub>0.06</sub>Co<sub>0.10</sub>O, and Zn<sub>0.81</sub>Mn<sub>0.09</sub>Co<sub>0.10</sub>O using Tauc's plot. The bandgap and crystallite size versus Mn content

They will then align along the direction of the field and entrapped by interface defects [49] thereby inducing SCP in the material. The grain boundary region will be electrically active due to the increase in the dielectric constant. At high frequency, species contributing to polarization are lagging behind the imposed field and this causes a decrease in  $\epsilon_r$ . In

addition, the interfacial area reduces with a decrease in the volume of particles such that RDP and SCP are increased. The density of oxygen vacancies increases in ZnO, Zn<sub>0.87</sub>Mn<sub>0.03</sub>Co<sub>0.10</sub>O, Zn<sub>0.84</sub>Mn<sub>0.06</sub>Co<sub>0.10</sub>O, and Zn<sub>0.81</sub>Mn<sub>0.09</sub>Co<sub>0.10</sub>O samples, and RDP, and SCP are enhanced. This shows that both size and doping concentration have influence dielectric property.



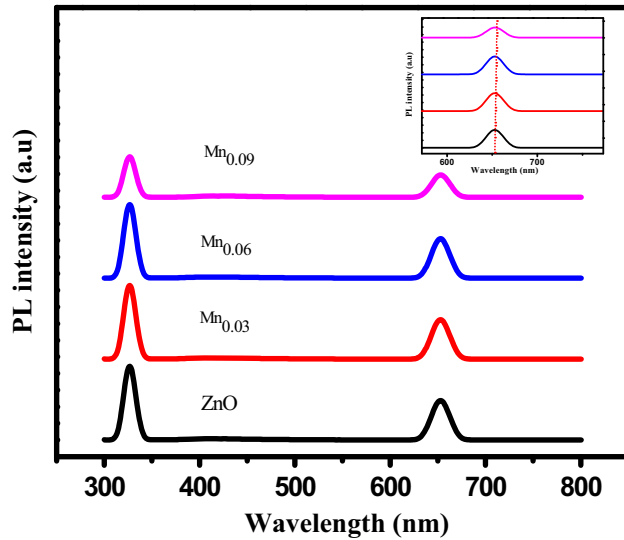


**Fig. 6** PL emissions spectra of ZnO,  $\text{Zn}_{0.87}\text{Mn}_{0.03}\text{Co}_{0.10}\text{O}$ ,  $\text{Zn}_{0.84}\text{Mn}_{0.06}\text{Co}_{0.10}\text{O}$  and  $\text{Zn}_{0.81}\text{Mn}_{0.09}\text{Co}_{0.10}\text{O}$

With the increase in Mn concentration, the  $\epsilon_r$  decreases in Co-ZnO calcined at 600 °C and this may result from some distortions emanating when smaller  $\text{Mn}^{2+}$  radii are substituting for  $\text{Zn}^{2+}$  as discussed in Refs. [33, 50].

Figure 8b shows that the dielectric loss for ZnO,  $\text{Zn}_{0.87}\text{Mn}_{0.03}\text{Co}_{0.10}\text{O}$ ,  $\text{Zn}_{0.84}\text{Mn}_{0.06}\text{Co}_{0.10}\text{O}$ , and  $\text{Zn}_{0.81}\text{Mn}_{0.09}\text{Co}_{0.10}\text{O}$  samples decreases with an increase in frequency and this may be due to space charge polarization. It is observed that cobalt and manganese doping in the ZnO matrix lowers the dielectric loss and increases the dielectric constant [33]. The relationship between frequency and dielectric loss at room temperature is shown in Fig. 8b. The dielectric loss exhibits a small peak-type behavior at the medium frequency and does not change at higher frequencies. The plots show that high dielectric loss is experienced at low frequencies, which may be explained by charge polarization according to the Shockley–Read mechanism [51]. Here, the surface electrons are captured by impurity ions in the matrix resulting in surface space charge polarization. The dielectric loss increases with an increase in frequency until a relaxation peak appears at the middle frequency before decreasing at higher frequencies (Fig. 8b). Relaxation peaks occur at the middle frequencies when the carrier's jumping frequency is almost equal to the external field.

Figure 8c shows the electrical conductivities of ZnO,  $\text{Zn}_{0.87}\text{Mn}_{0.03}\text{Co}_{0.10}\text{O}$ ,  $\text{Zn}_{0.84}\text{Mn}_{0.06}\text{Co}_{0.10}\text{O}$ , and  $\text{Zn}_{0.81}\text{Mn}_{0.09}\text{Co}_{0.10}\text{O}$  samples. Observations show that

the conductivity exponentially increases with an increase in frequency. Conductivity can be enhanced by either increasing the frequency of the applied field or dielectric relaxation at high frequencies. The latter effect is due to higher dielectric relaxation of polarization of nanoparticles in a high-frequency region. With an increase in dopants concentration, oxygen vacancies are produced, and these vacancies trap charge carriers, which are set free from these vacancies at higher frequencies resulting in high conductivities [33, 37]. The enhancement in conductivity can be described as when the frequency is low, transport follows infinite paths. Still, as the frequency increases, more and more charge carriers move along the applied field, and as a result, conductivity increases. This enhancement in conductivity is best explained by the hopping model, which occurs through the hopping of charge carriers between  $\text{Mn}^{2+}/\text{Mn}^{4+}$ ,  $\text{Co}^{2+}/\text{Co}^{3+}$  at high frequency due to enhanced mobility of charge carriers. The conductivity is maximum for  $\text{Zn}_{0.84}\text{Mn}_{0.06}\text{Co}_{0.10}\text{O}$  as in previous results; this sample possesses a small crystallite size, large strain and, hence maximum concentration of oxygen vacancies. The electrical conductivity  $\alpha_{a.c}$  of is given by Eq. 6.

$$\alpha_{a.c} = \epsilon_0 \epsilon_r \omega \tan \delta \quad (6)$$

With an increase in frequency, conductivity increases, while the dielectric loss decreases, and this is in agreement with the previous work [21]. (Mn, Co) co-doped ZnO nanoparticles could be useful for energy storage and gas sensing applications [38].

## 4 Summary

ZnO,  $\text{Zn}_{0.87}\text{Mn}_{0.03}\text{Co}_{0.10}\text{O}$ ,  $\text{Zn}_{0.84}\text{Mn}_{0.06}\text{Co}_{0.10}\text{O}$ , and  $\text{Zn}_{0.81}\text{Mn}_{0.09}\text{Co}_{0.10}\text{O}$  were successfully prepared and annealed. The properties were analyzed using several methods. The structure of the samples followed the wurtzite-type structure due to the proper accommodation of dopants. In the presence of small concentrations of dopants, weak ferromagnetism was observed, and it becomes strong with an increase in manganese ions. Enhancement of ferromagnetism to produce DMS materials was explained based on BMPs caused by a large number of oxygen vacancies introduced to ZnO lattice with the incorporation of Manganese and Cobalt ions. Furthermore, the samples' dielectric measurements demonstrated a

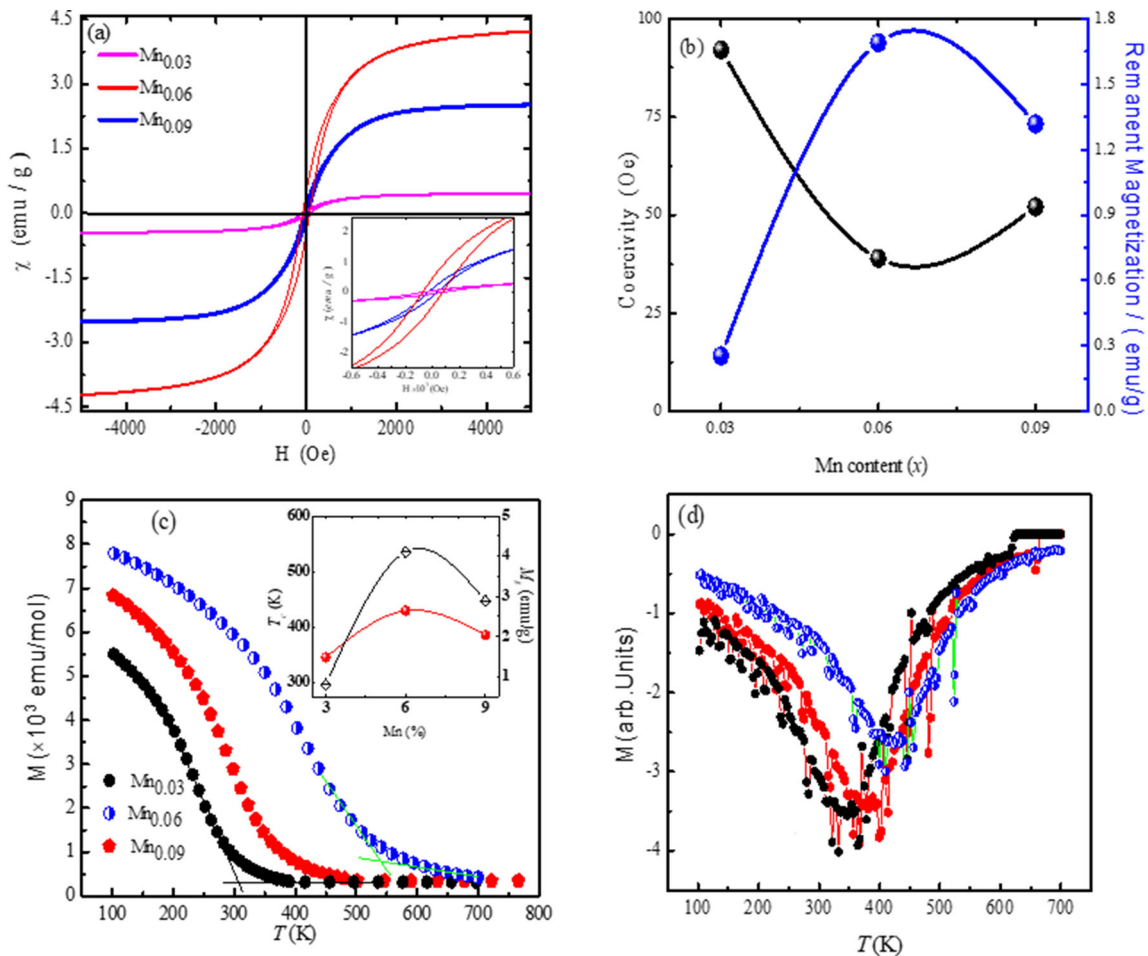


**Fig. 7** **a** Hysteresis loop (inset shows the  $M-H$  curve near zero magnetic field), and **b** their corresponding coercivity, and remanent magnetization, **c** temperature dependence magnetization (inset of (c) shows the remanent magnetization

and Curie temperature ( $T_C$ ) versus Mn content) and **d** the corresponding  $1/M$  versus temperature of the  $\text{Zn}_{0.87}\text{Mn}_{0.03}\text{Co}_{0.10}\text{O}$ ,  $\text{Zn}_{0.84}\text{Mn}_{0.06}\text{Co}_{0.10}\text{O}$ , and  $\text{Zn}_{0.81}\text{Mn}_{0.09}\text{Co}_{0.10}\text{O}$  samples

decrease in dielectric constant with incorporation of manganese ions in the structure. An increase in electrical conductivity is attributed to the increase in charge density (charges liberated from oxygen

vacancies along with conduction charge carriers) at higher frequencies. It reveals that co-doping is useful in modifying the properties of the samples.

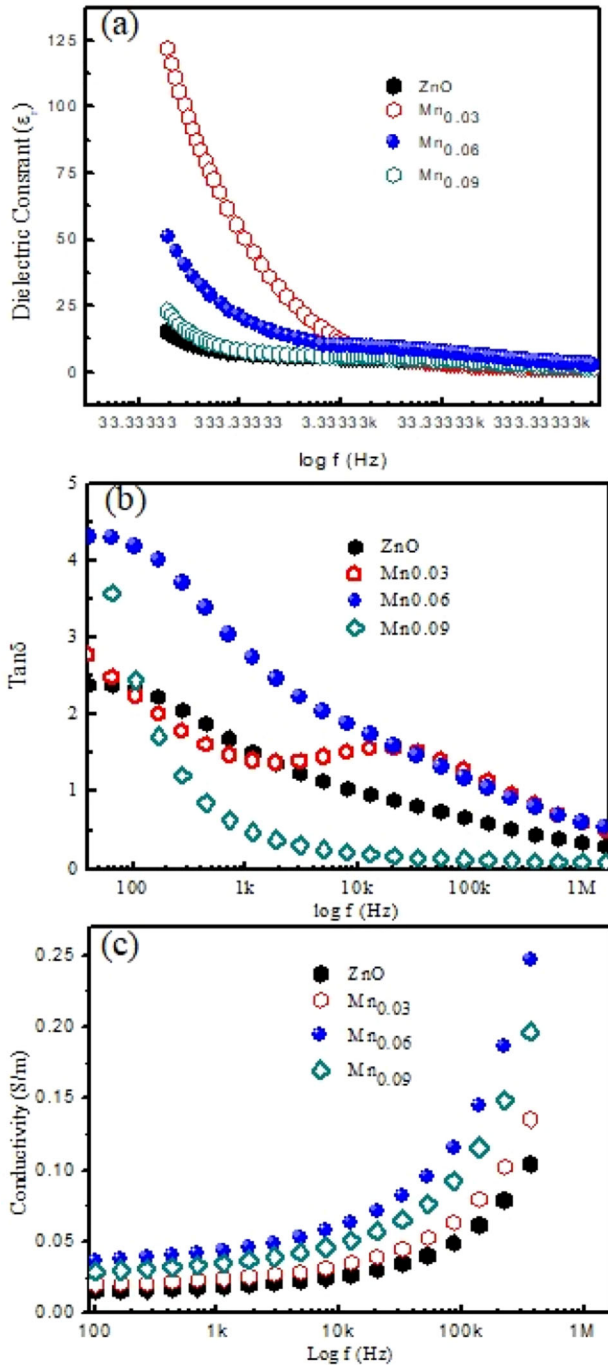


**Fig. 8** a Dielectric constant, b dielectric loss, and c electrical conductivity versus frequency of ZnO,  $\text{Zn}_{0.87}\text{Mn}_{0.03}\text{Co}_{0.10}\text{O}$ ,  $\text{Zn}_{0.84}\text{Mn}_{0.06}\text{Co}_{0.10}\text{O}$ , and  $\text{Zn}_{0.81}\text{Mn}_{0.09}\text{Co}_{0.10}\text{O}$  nanoparticles at room temperature

## References

1. Q. Wang, Q. Sun, P. Jena, *Phys. Rev. B* **75**, 035322 (2007)
2. C. Klingshirn, *Phys. Status Solidi B* **71**, 547 (1975)

3. Y. Chang, D. Wang, X. Luo, X. Xu, X. Chen, L. Li, C. Chen, R. Wang, J. Xu, D. Yu, *Appl. Phys. Lett.* **83**, 4020 (2003)
4. Y. Ohno, F. Matsukura, H. Ohno, D.D. Awschalom, *Nature* **402**, 790 (1999)
5. S. Wolf, D. Awschalom, R. Buhrman, J. Daughton, V.S. von Molnár, M. Roukes, A.Y. Chtchelkanova, D. Treger, *Science* **294**, 1488 (2001)
6. A. Fert, *Angew. Chem. Int. Ed.* **47**, 5956 (2008)
7. T. Dietl, H. Ohno, *Science* **287**, 1019 (2000)
8. X. Xu, C. Cao, *J. Magn. Magn. Mater.* **321**, 2216 (2009)
9. K. Sato, H. Katayama-Yoshida, *Jpn. J. Appl. Phys.* **39**, L555 (2000)
10. T. Dietl, H. Ohno, F. Matsukura, J. Cibert, E.D. Ferrand, *Science* **287**, 1019 (2000)
11. P.K. Sharma, R.K. Dutta, A.C. Pandey, *J. Magn. Magn. Mater.* **321**, 4001 (2009)
12. G.Y. Ahn, S.-I. Park, C.S. Kim, *J. Magn. Magn. Mater.* **303**, e329 (2006)
13. S.Y. Bae, C.W. Na, J.H. Kang, J. Park, *J. Phys. Chem. B* **109**, 2526 (2005)
14. J. Wen, J. Lao, D. Wang, T. Kyaw, Y. Foo, Z. Ren, *Chem. Phys. Lett.* **372**, 717 (2003)
15. A. Ishizumi, Y. Kanemitsu, *Appl. Phys. Lett.* **86**, 253106 (2005)
16. J. Chen, M. Yu, W. Zhou, K. Sun, L. Wang, *Appl. Phys. Lett.* **87**, 173119 (2005)
17. Y. Chen, Y. Liu, S. Lu, C. Xu, C. Shao, C. Wang, J. Zhang, Y. Lu, D. Shen, X. Fan, *J. Chem. Phys.* **123**, 134701 (2005)
18. L. Yang, X. Wu, T. Qiu, G. Siu, P.K. Chu, *J. Appl. Phys.* **99**, 074303 (2006)
19. R. Khan, C.I.L. de Araujo, T. Khan, S.A. Khattak, E. Ahmed, A. Khan, B. Ullah, G. Khan, K. Safeen, A. Safeen, *J. Mater. Sci.* **30**, 3396 (2019)
20. R. Khan, S. Fashu, *J. Mater. Sci.* **28**, 10122 (2017)
21. S. Tanaka, A. Makiya, Z. Kato, K. Uematsu, *J. Eur. Ceram. Soc.* **29**, 955 (2009)
22. T.S. Suzuki, T. Uchikoshi, Y. Sakka, *Sci. Technol. Adv. Mater.* **7**, 356 (2006)
23. D. Molodov, P. Konijnenberg, *Scripta Mater.* **54**, 977 (2006)
24. R. Khan, S. Fashu, Z.U. Rehman, A. Khan, M.U. Rahman, *J. Mater. Sci.* **29**, 32 (2018)
25. X. Zeng, V. Pelenovich, A. Ieshkin, A. Danilov, A. Tolstogouзов, W. Zuo, J. Ranjana, D. Hu, N. Devi, D. Fu, *Rapid Commun. Mass Spectrom.* **33**, 1449 (2019)
26. J. Wojnarowicz, M. Omelchenko, J. Szczytko, T. Chudoba, S. Gierlotka, A. Majhofer, A. Twardowski, W. Lojkowski, *Crystals* **8**, 410 (2018)
27. B. Babić-Stojić, D. Milivojević, J. Blanuša, V. Spasojević, N. Bibić, B. Simonović, D. Arandelović, *J. Phys.* **20**, 235217 (2008)

28. P. Lommens, K. Lambert, F. Loncke, D. De Muynck, T. Balkan, F. Vanhaecke, H. Vrielinck, F. Callens, Z. Hens, *ChemPhysChem* **9**, 484 (2008)
29. J. Beltrán, J. Osorio, C. Barrero, C.B. Hanna, A. Punnoose, J. *Appl. Phys.* **113**, 17C308 (2013)
30. N.M. Basith, J.J. Vijaya, L.J. Kennedy, M. Bououdina, S. Jenefer, V. Kaviyarasan, J. *Mater. Sci. Technol.* **30**, 1108 (2014)
31. L. Yang, X. Wu, G. Huang, T. Qiu, Y. Yang, J. *Appl. Phys.* **97**, 014308 (2005)
32. K. Rajwali, F. Ming-Hu, *Chin. Phys. B* **24**, 127803 (2015)
33. R. Khan, C.I.L. de Araujo, T. Khan, A. Khan, B. Ullah, S. Fashu, J. *Mater. Sci.* **29**, 9785 (2018)
34. H. Nasir, N. Rahman, Zulfiqar et al., Variations in structural, optical, and dielectric properties of CuO nanostructures with thermal decomposition. *J. Mater. Sci.* **31**, 10649–10656 (2020)
35. S. Fabbiyola, L.J. Kennedy, A. Dakhel, M. Bououdina, J.J. Vijaya, T. Ratnaji, *J. Mol. Struct.* **1109**, 89 (2016)
36. V. Gandhi, R. Ganesan, H.H. Abdulrahman Syedahamed, M. Thaiyan, *J. Phys. Chem. C* **118**, 9715 (2014)
37. M. Alijani, N.N. Ilkhechi, *Silicon* **10**, 2569 (2018)
38. K.R. Kittilstved, D.A. Schwartz, A.C. Tuan, S.M. Heald, S.A. Chambers, D.R. Gamelin, *Phys. Rev. Lett.* **97**, 037203 (2006)
39. Y. Lin, D. Jiang, F. Lin, W. Shi, X. Ma, *J. Alloy Compd.* **436**, 30 (2007)
40. Z. Tian, S. Yuan, J. He, P. Li, S. Zhang, C. Wang, Y. Wang, S. Yin, L. Liu, *J. Alloy Compd.* **466**, 26 (2008)
41. C. Gao, F. Lin, X. Zhou, W. Shi, A. Liu, *J. Alloy Compd.* **565**, 154 (2013)
42. S. Qi, F. Jiang, J. Fan, H. Wu, S. Zhang, G.A. Gehring, Z. Zhang, X. Xu, *Phys. Rev. B* **84**, 205204 (2011)
43. K.C. Verma, R. Kotnala, *Phys. Chem. Chem. Phys.* **18**, 5647 (2016)
44. S.V. Vegesna, V.J. Bhat, D. Bürger, J. Dellith, I. Skorupa, O.G. Schmidt, H. Schmidt, *Sci. Rep.* **10**, 1 (2020)
45. R. Khan, S. Fashu, *J. Mater. Sci.* **28**, 4333 (2017)
46. S.U. Haq, S.A. Khattak, T. Jan, R. Khan, I. Ullah, T. Khan, S.K. Shah, G. Khan, R. Ahmad, *Mater. Res. Express* **6**, 115037 (2019)
47. D. Karmakar, S. Mandal, R. Kadam, P. Paulose, A. Rajarajan, T.K. Nath, A.K. Das, I. Dasgupta, G. Das, *Phys. Rev. B* **75**, 144404 (2007)
48. R. Khan, S. Fashu, Y. Zaman, *J. Mater. Sci.* **27**, 5960 (2016)
49. D.R. Clarke, *J. Am. Ceram. Soc.* **82**, 485 (1999)
50. R. Khan, M.U. Rahman, Z. Iqbal, *J. Mater. Sci.* **27**, 12490 (2016)
51. C.B. Ong, L.Y. Ng, A.W. Mohammad, *Renew. Sustain. Energy Rev.* **81**, 536 (2018)

**Publisher's Note** Springer Nature remains neutral with regard to jurisdictional claims in published maps and institutional affiliations.